Title: Three-dimensional morphology of the vibrissal array of the harbor seal (*Phoca vitulina*)

Running Title: Vibrissae of the harbor seal

Authors: Matthew M. Graff[1]
Hayley M. Belli[2†]
Sven Wieskotten[3††]
Yvonne Krüger[3]
Guido Dehnhardt[3]
Mitra J.Z. Hartmann[1, 2]

Affiliations: [1] Department of Mechanical Engineering, Northwestern University, Evanston, Illinois, 60208

[2] Department of Biomedical Engineering, Northwestern University, Evanston, Illinois, 60208

[3] Institute for Biosciences, University of Rostock, Rostock, Germany

[†] Present address:
Department of Population Health, Biostatistics Division
New York University Grossman School of Medicine
New York, NY, 10016

[††] Present address:
Animal and Training
Postcode 30 10 43
18111 Rostock

Corresponding Author:

Mitra J.Z. Hartmann
Mechanical Engineering Department
Northwestern University
2145 Sheridan Rd
Evanston, IL 60208
hartmann@northwestern.edu
Tel: 847-467-4633

KEYWORDS: comparative anatomy, flow sensing, trigeminal, whisker, somatosensory, touch

SUMMARY STATEMENT: We quantify the three-dimensional position and orientation of the whiskers across the face of the harbor seal and discuss how this geometrical arrangement could aid in flow sensing and touch.

Abstract:
Nearly all mammals have specialized facial hairs known as vibrissae (whiskers) that serve a variety of functions, including tactile exploration and flow sensing. The geometric arrangement of the whiskers on an animal's face as well as each whisker's individual geometry will play a critical role in determining the sensory information that the animal acquires. To date, however, the relationships between vibrissal morphology and functional use remain largely unexplored. In the present work, we quantify the three-dimensional morphology of the vibrissal array of the harbor seal (*Phoca vitulina*). Specifically, we develop relationships between a whisker's basepoint location and its arc length, its intrinsic curvature, and the angles at which it emerges from the mystacial pad. Results show that the arc length of seal whisker ranges between 20 – 120 mm, and the shape of a seal whisker is well-described by a cubic equation. The orientation at which each whisker emerges from the seal's face can be described by three angles. The angle of emergence in the horizontal plane depends on both the whisker's dorsal-ventral as well as its rostral-caudal basepoint location. In contrast, the angle of emergence in the elevation plane depends only on the whisker's dorsal-ventral basepoint location. Finally, the angle that the whisker "twists" about its own axis again depends on both dorsal-ventral and rostral-caudal basepoint location. We discuss how the morphology of the array could create a range of mechanical responses specialized for tactile or flow sensing.

1. Introduction

Nearly all mammals have specialized hairs known as vibrissae (whiskers) that protrude from the mystacial pad in a regular grid-like pattern (Grant et al., 2013b; Muchlinski, 2010; Welker, 1964). The vibrissal arrays of different species have distinct shapes, sizes, and arrangements (Brecht et al., 1997; Danforth, 1925; Grant et al., 2013b; Muchlinski, 2010). The arrays of some species are only sparsely populated with whiskers, while others are densely packed; for example, bats typically have fewer than ten macrovibrissae per array, while shrews have nearly 80 (Muchlinski, 2010).

Different species also vary in their ability to "whisk," a behavior in which the animal moves its whiskers independently of its head (Grant et al., 2013b; Jin et al., 2004). Rats and mice can generate exceptionally strong whisking behaviors, with specialized intrinsic muscles allowing whisker rotations up to ~60 degrees (Grant et al., 2009; Haidarliu et al., 2017; Haidarliu et al., 2015; Haidarliu et al., 2010; Haidarliu et al., 2011; Hill et al., 2008; Hobbs et al., 2016; Towal and Hartmann, 2008). In contrast, animals such as cats and seals have "mobile" whiskers, allowing them to adjust overall whisker protraction on both sides of the face, but exhibit minimal whisking behavior (Dehnhardt and Kaminski, 1995; Grant et al., 2013b; Woolsey et al., 1975).

These species-related differences in whisker morphology and whisking ability seem likely to be associated with differential functional use of the whiskers. For example, many rodents use direct tactile signals from the whiskers to explore the environment in complex ways, including climbing (Arkley et al., 2014) and locomotion (Arkley et al., 2014; Grant et al., 2018; Grant et al., 2012). In contrast, seals primarily use their whiskers to track wakes while hunting fish (Dehnhardt et al., 1998; Dehnhardt et al., 2001; Hyvarinen, 1989; Kruger et al., 2018; Miersch et al., 2011; Schulte-Pelkum et al., 2007; Wieskotten et al., 2010; Wieskotten et al., 2011) though they can also use them in tactile discrimination tasks (Dehnhardt and Kaminski, 1995; Grant et al., 2013a).

To date, however, the relationships between vibrissal array morphology and functional use remain largely unexplored. In the present work, we employ a standardized approach (Belli et al., 2018) to quantify the morphology of the whisker array of the harbor seal. The approach accommodates for different numbers and arrangements of whiskers by using the three-dimensional (3D) locations of the whisker basepoints as parameters to quantify the remainder of the morphology of the array. Specifically, equations are developed that relate the whisker basepoint locations to whisker arc length, curvature, and the 3D angles at which the whiskers emerge from the animal's face.

We anticipate that this work will help clarify the mechanical basis by which seal vibrissae enable efficient wake detection and following, as well as more generally serve as a starting point for quantitative comparisons of vibrissal arrays across species.

2. Methods

Three adult, male harbor seals were used. All of the seals resided at the Marine Science Center of Rostock University in Hohe Düne, Germany, and all experiments were carried out in accordance with the European Communities Council Directive of 24 November 1986 (86/609/EEC), the directive 2010/63/EU and the Directive of the §7 and §11 TierSchG of the German Protection of Animals Act (Tierschutzgesetz)

2.1 Data acquisition

The head and vibrissal array of each seal were scanned using a (3D) volumetric scanner. A total of 361 3D whisker images were taken of 171 unique whiskers. Additionally, 127 two dimensional (2D) images were taken of 52 unique whiskers.

Three-dimensional volumetric scanning and data extraction: A Konica Minolta Vivid 900 non-contact, 3D laser scanner was used to acquire 3D scans. Each seal was trained to pose its head on a semicircular stand (a chinrest) for a duration of less than one minute (one to two scans). The seal's eyes were covered with a thick, opaque rubber mask during laser scanning. An example of a blindfolded seal resting its head on the chinrest is shown in Fig. 1A. The scanner output was a digitized point cloud. The software package Rapidform™ XOR2 was used to control the scanner from a laptop computer. The point clouds included portions of the seal's head, neck, and whiskers. The seal's head and whisker arrays were larger than the field of view of the scanner, so multiple scans in several orientations were taken and then combined in post processing.

Two-dimensional photographs: Because whiskers could not be plucked from the animal, photographs of the whiskers were taken against a black, hard-plastic background. A camera-frame system (Fig. 1B) was built in order to ensure that the whiskers lay flat on the background with no distortion of their natural shape. The frame system, constructed of 80/20®, also ensured a fixed distance between the camera (Panasonic, Lumix DMC-FZ20) and the background. Length scales (thin plastic rulers) were affixed rigidly to the background.

The 2D photographic procedure was as follows: A select number of whiskers were marked using non-toxic watercolor paint. The background was then manually held against the face of the seal in an orientation such that one selected whisker lay flat against the background without any shape distortion. Although several whiskers (painted different colors) were often visible in each photo, the frame was oriented so that one specific whisker lay completely flat. An example of a typical 2D photo of a whisker with a blue stripe is shown in Fig. 1C. The photo in Fig. 1D shows how the frame was oriented by hand to position the whisker onto the background.

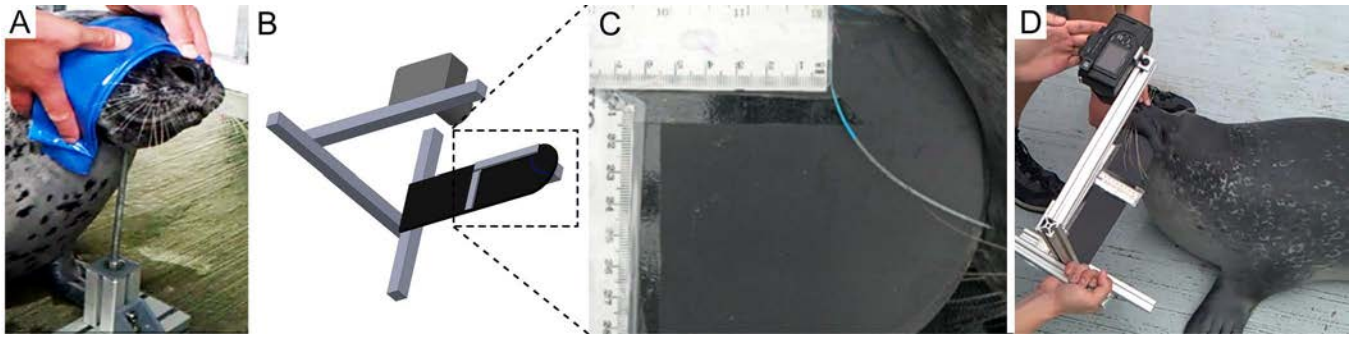

Fig. 1: The head and vibrissal array of a seal were scanned in 3D and 2D. A) A blindfolded seal is shown perching its head on a chinrest to permit 3D laser scanning. The photo has been brightened and contrast enhanced to improve visual clarity. **B)** A schematic of the custom-built camera frame system, which allowed the whisker to be photographed in 2D. The orientation of the background was manually adjusted so that the whisker of interest lay flat on the background. **C)** An expanded view of the camera frame system shows an example of 2D photograph of a whisker identified with non-toxic water color paint. **D)** A photo shows how the custom-built camera frame system was used in practice.

A log of the correspondence between painted color and whisker identity was recorded as the photographs were taken, and the images of the seal whiskers were then imported into Matlab™ (The Mathworks, Natick, MA) for measurement. The shapes of the whiskers were manually extracted by clicking on the center of the whisker along its length, from base to tip. After clicking along the entire whisker, the traces were up-sampled (linear interpolation) to contain 100 points and smoothed using a moving average filter with a window size of 15 samples. All whisker traces were overlaid onto the original photographs and manually inspected for accuracy. All traces were converted to real-world length units using the scale bars attached to the background (Fig. 1C).

2.2 Alignment of three-dimensional data

Alignment of the 3D data required three basic steps.

First, in order to assign identities to each of the whiskers, we performed a coarse alignment of the point clouds within Rapidform™. Data points associated with the head or neck, or with scanner noise were manually removed. The most complete point cloud for each seal was chosen as the reference scan. All other scans were rotated and translated to align to the reference scan using facial landmarks. Landmarks included whisker basepoints, the nostrils, and creases in the face and mouth. Whiskers were identified by their location within the array (Dehnhardt and Kaminski, 1995) as well as by comparing the point clouds to photographs of the full mystacial pad of the seal. All data points corresponding to each individual whisker were saved into their own point clouds.

Second, we localized the basepoints of all identified whiskers. For each whisker point cloud, the basepoint was identified by finding the intersection between the whisker and the skin in Rapidform™. In nearly all cases the proximal portion of the whisker and the skin were both clearly visible. In the event that the basepoint was not identifiable in a particular whisker scan, that scan was removed from the dataset and not used for further analysis. The whisker-skin intersection of the point cloud was typically composed of 5 to 15 points. The centroid of these points was used as the basepoint location.

At this point in the alignment process, each 3D scan of a particular seal now consists only of point clouds of identified whiskers, and each whisker point cloud has an average basepoint. All non-whisker related points have been removed.

The third step was to perform fine alignment of these “whisker-only” scans. As before, the scan with the largest number of basepoints was used as the reference scan. An optimization was performed using the “fminsearch” function in Matlab™ in which each of the “whisker-only” scans was rotated and translated into alignment with the reference scan. The objective function for the minimization consisted of the summed distances of all matching basepoints between the reference scan and each individual scan.

2.3 Standard position and orientation of the head

The whisker arrays of different species align differently with respect to facial features such as the eyes, nostrils, and ears, and may also align differently with respect to the skull landmarks bregma and lambda. We therefore developed an approach to define the standard position and orientation of any animal’s head and vibrissal array using only the locations of the whisker basepoints (Belli et al., 2018). The advantage of this approach is that all information required to align the array is inherent within the whisker measurements. This procedure can thus be applied to any whiskered species regardless of the presence or absence of any particular facial or skull landmark.

To place the head into the standard position, we translated the aligned point clouds so that the origin was located at the mean position of all right and left whisker basepoints. This puts the origin inside the animal’s head, near the center of the muzzle (Fig. 2A). This procedure was implemented using “matched” basepoints between right and left sides; in the case that a basepoint was missing on one side, its non-missing complement was omitted from the calculation of the origin. For seals with multiple measurements of the same basepoint, the mean of the points was used for the alignment procedures.

To put the head into the standard orientation we performed a roll-yaw-pitch (y-z-x-axis) rotation sequence. The roll rotation (about the y-axis) and the yaw rotation (about the z-axis) placed the center of the right array on the

positive x-axis and the center of the left array on the negative x-axis (Fig. 2A). The "center" of the right (left) array is defined as the mean of all basepoint positions on the right (left) side of the animal.

The pitch rotation (about the x-axis) aligned the average whisker row plane with the x-y (horizontal) plane. To find the average whisker row plane, individual planes were fit to the basepoints of the combined left and right whisker rows using least squares and producing six normal vectors – one for each of the six whisker rows B - G. The A row of whiskers was excluded because it contained an insufficient number of points to define a plane. The maximum sum-squared-error between the basepoints and its fitted plane was 90.2 mm^2 (maximum residual was 5.5 mm). The mean of the unit normal vectors describes the average row plane (Fig. 2B). The animal's head was then pitched about the x-axis so that the average row plane was parallel with the x-y plane. The final position of the seal point cloud is shown in Fig. 2C.

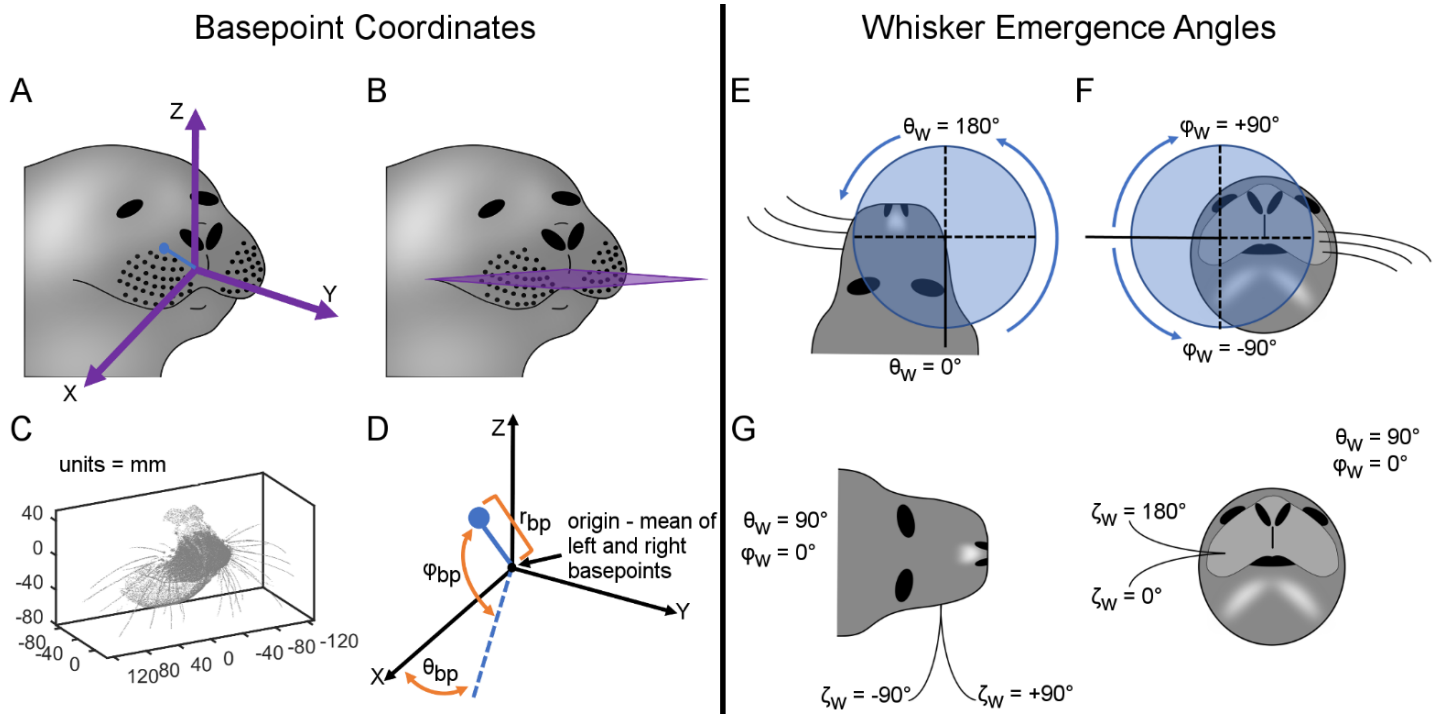

Fig. 2: Coordinate systems for whisker basepoints and emergence angles are defined in schematics. A) Schematic of the standard position and orientation of the vibrissal array. The origin (0,0,0) is placed at the mean position of the basepoints of the left and right array. The right basepoints surround the positive x-axis. The blue line and dot indicate a single example of a basepoint location, for comparison with panel (D). **B)** The horizontal (x-y) plane is defined by the average row plane of the basepoints. **C)** An example point cloud of the seal face in the standard position and orientation. **D)** Each basepoint location is described in spherical coordinates (θ_{bp}, φ_{bp}, r_{bp}). The angle θ_{bp} ranges from -90° (caudal) to +90° (rostral), where θ_{bp} = 0° lies in the x-z plane. The angle φ_{bp} ranges from -90° (ventral) to +90° (dorsal), where φ_{bp} = 0° lies in the x-y plane. The basepoint coordinates of one example whisker (blue dot) are shown. **E)** The variable θ_w describes the rostrocaudal angle at which the proximal, approximately-linear portion of the whisker emerges from the mystacial pad. Values range from 0° to 360°. **F)** The variable φ_w describes the dorsoventral angle at which the proximal, approximately-linear portion whisker emerges from the mystacial pad. Values range from -90° to 90°. **G)** The variable ζ_w describes the orientation of the whisker about its own axis. Values range between ±180°.

2.4 Coordinates of the whisker basepoints with the head in standard position and orientation

The seal's whisker array is organized in a grid-like pattern that includes 7 rows and 9 columns (Dehnhardt and Kaminski, 1995) In contrast, the rat's whisker array is organized in a grid-like pattern that includes 5 rows and 7 columns (Belli et al., 2018; Brecht et al., 1997; Knutsen et al., 2008; Towal et al., 2011). For both the seal and the rat, a whisker is identified with a letter to indicate its row and a number to indicate its column. In the present study, however, we chose to quantify the morphology of the seal whisker array in terms of the coordinates of the whisker basepoints, rather than row and column identity.

Basepoint coordinates were determined within a spherical coordinate system (Fig. 2D) with the origin located at the mean position of all the basepoint locations (Fig. 2B). For each whisker, the variable θ_{bp} describes the rostro-caudal location of the basepoint with respect to the positive x-axis. A positive value of θ_{bp} indicates that the whisker is more rostral, while a negative angle indicates that the whisker is more caudal. The variable φ_{bp} describes the dorsoventral location of the basepoints with respect to the x-y plane. A positive value of φ_{bp} indicates a more dorsal basepoint location, while a negative coordinate indicates a more ventral basepoint location. The third basepoint coordinate is the radius (r_{bp}), i.e., the straight-line distance between the origin and the basepoint. Scaling the basepoint radii scales the size of the seal's face.

For mathematical simplicity, whisker arrays on the left side were converted to right side arrays by mirroring them across the y-z plane. All equations and figures are presented in terms of whisker arrays on the right side. The advantage of this choice of coordinate systems is that it intuitively exploits the bilateral symmetry of the array.

2.5 Measurements of whisker arc length and intrinsic curvature using two-dimensional data

The length of a whisker is described by its arc length (S), defined as the total length of the whisker measured along its arc length. Using the 2D photographs, the arc length of each whisker was calculated by summing the lengths of the segments that composed the traced image.

As will be shown in *Results*, the 2D shape of a seal whisker is best described by a cubic equation, and its intrinsic curvature can be described with a single "curvature coefficient." In its most general form, a cubic polynomial has four coefficients: $f(x)=Ax^3 + Bx^2 + Cx + D$. For simplicity, we forced the B, C, and D coefficients to exactly equal zero, and performed a least-squares regression to the curve $f(x)=Ax^3$. This procedure offers the advantage that only a single coefficient is required to describe the intrinsic curvature of the whisker, making it easier to compare different whisker shapes. A similar approach was used in previous studies to parameterize the rat vibrissal array (Belli et al., 2018; Knutsen et al., 2008; Towal et al., 2011). Note, however, that while rat whiskers are typically fit by a quadratic function, seal whiskers are more naturally described by a cubic function.

This alignment procedure requires the proximal portion of the whisker to be aligned with the x-axis. To achieve this alignment, the whisker was first divided into 100 nodes. The whisker basepoint was then placed at the origin (0,0) and the next proximal mode (~1% of the whisker arc length) was aligned with the x-axis.

2.6 Angles of emergence

The orientations of the whiskers as they emerge from the mystacial pad are called the angles of emergence. In the present work, we describe the whiskers using Euler angles (specifically Tait-Bryan angles) applicable to the right array.

The angle θ_w describes the rostrocaudal orientation of the proximal portion of the whisker. A θ_w angle of 180° is directed rostrally while an angle of 0° is directed caudally (Fig. 2E). The angle φ_w describes the elevation of the proximal portion of the whisker. A φ_w angle of 90° points the whisker dorsally while an angle of -90° points it ventrally (Fig. 2F). Whiskers have an intrinsic curvature and therefore they require a third angle, ζ_w, to describe the roll about their own axis. For a whisker with θ_w=90° and φ_w=0°, a ζ_w angle of 90° will curve concave forward and -90° concave backward (Fig. 2G). In contrast, a ζ_w angle of 180° will curve concave upward, and 0° concave downward (Fig. 2H). Note that the directionality of the whisker's concavity in the laboratory frame is defined by all three orientation angles, not just ζ_w.

Similar to the basepoint coordinates, the angles of emergence are defined only for whiskers of the right array. For simplicity, all left side whisker arrays were converted to right side arrays by reflecting them across the y-z plane.

An optimization was performed using the built-in Matlab™ function "fmincon" to calculate the angles of emergence. The parameters for the optimization were θ_w, φ_w, ζ_w, along with S and A. Constraints on the angles of emergence in the optimization were: θ_w=[0, 360], φ_w =[-90, 90], ζ_w =[-180, 180], S = [straight distance from base to tip, lower bound + 50mm], curvature coefficient A=[0 to 1]. The curvature coefficient A was constrained to lie between 0 and 1. The lower bound for S was chosen to be the linear distance between the base and tip (the smallest S could ever possibly be to connect those two points) and 50 mm longer than the lower bound.

Beginning with the whisker point cloud in standard position and orientation (Fig 2A-C), the individual points within the cloud were sorted by distance from the basepoint.

Their x, y, z coordinates were then smoothed with a moving average filter (window size of five samples). The whisker was resampled into 500 micron segments and translated to have the base at the origin . The routine subsequently varied five variables, θ_w, φ_w, ζ_w, S, and A to fit an idealized whisker model to the whisker point cloud. The idealized model started with the base at the origin (θ_{bp}= 0, φ_{bp} =0, r_{bp} =0), and the proximal section of the whisker was coaxial to the negative y-axis (θ_w=0, φ_w=0). The model's orientation was concave down (ζ_w=0). To align the idealized model with the whisker point cloud, an Euler rotation sequence was performed. The order of the rotations was y-axis (roll, ζ_w), x-axis (pitch, φ_w), z-axis (yaw, θ_w). All rotations were extrinsic around the global y-x-z axes. Additionally, the arc-length and curvature were optimized to best match the idealized model to the point cloud. The optimization's objective function minimized the mean sum squared distance between the whisker point cloud and the points in the idealized whisker model.

2.7 Developing equations for morphological parameters; statistical analysis

We aimed to develop equations that relate whisker arc length (S), intrinsic curvature (A), the angles of emergence (θ_w, φ_w, ζ_w) and the radial distance of each base point (r_{bp}) to the locations of the whisker basepoints θ_{bp} and φ_{bp}.

2.7.1. Arc length and intrinsic curvature as functions of θ_{bp} and φ_{bp}

The procedures described in sections 2.1 to 2.6 yielded a total of 171 unique 3D images of whiskers from three individual seals. However, when these 171 whiskers were compared across individuals, several whiskers were found to have unusually short arc lengths given their identity. The short arc length was attributable to two causes. First, in some scans, the 3D scanner did not capture the full length of the whisker. Second, we performed the scans during the summer months, when two seals were molting (Hirons et al., 2001) and some of the whiskers had not fully regrown.

Rather than fit a model that under-predicts S and inaccurately predicts A, we excluded the data for S and A from the 3D scans, and instead constructed multivariate linear regressions models for S and A as functions of θ_{bp} and φ_{bp} using only the 2D dataset of 52 unique whiskers. For these 2D data, scan quality did not contribute significantly to measurement error in the arc length, as was the case for the 3D scans. The unusually short 2D measurements were attributable only to molting. To determine outliers due to molting, any whisker from the 2D data (from a particular seal) that was more than 30 mm shorter than the longest whisker (across all seals, for that whisker identity) was excluded. Eight of the 52 2D traces were excluded based on this criterion, and the remaining 44 2D whiskers were then used to find relationships between S, A and θ_{bp} and φ_{bp}.

Among the 44 whiskers used in constructing the 2D model, 27 came from Seal 1, 13 from Seal 2, and four from Seal 3. Using the reduced set of 44 whiskers, first-order models for the log-transformed 2D arc length (S) and cubic coefficient (A) were fit as functions of θ_{bp} and φ_{bp}. Because 2D traces did not provide basepoint coordinate measurements, the average basepoint coordinates from the 3D scans were matched to the whisker identity of each 2D trace.

Even though there are fewer 2D measurements than 3D measurements for S and A, we can be confident that they capture the full length of the whisker and will therefore more accurately depict the cubic coefficient. Therefore, results for arc length and cubic coefficient (Figure 5 and equations 2, 3, and 4) are based only on the 2D data.

2.7.2. Angles of emergence (θ_w, φ_w, and ζ_w) and r_{bp} as functions of θ_{bp} and φ_{bp}

As described above, some of the whiskers from the 3D images were found to have unusually short arc lengths. However, we did not remove any whiskers when finding equations for θ_w, φ_w, ζ_w, and r_{bp} as functions of θ_{bp} and φ_{bp}, because we fully expect whiskers at various stages in the growth cycle (i.e., with various lengths) to retain their validity for these parameters.

We aimed to construct multivariable linear regression models for r_{bp}, θ_w, φ_w, and ζ_w as functions of θ_{bp} and φ_{bp}. Rather than fit a model directly to the entire dataset of 171 whiskers and potentially overfit the data, we wanted

to first find the lowest order model that could fit all three seals individually, and then apply a model of same order to the entire dataset of 171 whiskers.

We divided the data from 171 whiskers for r_{bp}, θ_w, φ_w, and ζ_w into three subgroups by seal identity. For each of the three seals, we made histograms for r_{bp}, θ_w, φ_w, and ζ_w. All 12 histograms were found to be normally distributed. Linear regression models were constructed for each seal to test whether r_{bp}, θ_w, φ_w, and ζ_w were univariately associated with θ_{bp} and/or φ_{bp}. We tested the hypothesis that the θ_{bp} and/or φ_{bp} regression coefficients were equal to zero. If the p-value for each independent variable coefficient was less than or equal to 0.05, a second order model (square of θ_{bp} and/or square of φ_{bp}) was applied and again we tested the hypothesis that the regression coefficients for these quadratic order terms was equal to zero. If the p-value was greater than 0.05 for each second order coefficient in the model, the model remained first order. A third order model (cube of θ_{bp} and/or cube of φ_{bp}) was fit if the p-value was less than 0.05, and the process was repeated. We did not find any models for whiskers from an individual seal to have independent variable predictors greater than third-order.

Using the procedure described above, the lowest order model among the three seals with significant regression coefficients was selected as the final model. As will be shown in the results, we found r_{bp}, θ_w and ζ_w to be linear in both θ_{bp} and φ_{bp}, and φ_w to be linear in φ_{bp} only. These final selected models were fit to the entire combined dataset of 171 whiskers across all three seals.

3. Results

3.1. Motivation and description of variables: comparison with previous studies in the rat

Previous work in the rat has shown that the general morphology of a vibrissal array can be quantified in terms of eight parameters (Belli et al., 2018; Towal et al., 2011). The first two parameters describe each whisker's two-dimensional (2D) geometry. When removed from the rat's face, a whisker is mostly planar, with a 2D shape that closely approximates a parabola (Belli et al., 2018; Knutsen et al., 2008; Quist and Hartmann, 2012; Towal et al., 2011). The whisker's shape can be described by its arc length (S) and its intrinsic curvature (A). After choosing an origin and a horizontal plane, each 2D whisker can then be positioned and oriented on the rat's face using six additional parameters. Those six parameters are the basepoint (bp) of the whisker, defined in spherical coordinates (r_{bp}, θ_{bp}, φ_{bp}), and the orientation of the whisker, defined by three Euler angles (θ_w, φ_w, ζ_w) and a convention for the order of rotation.

Initial work on the rat found equations that fit each of these eight parameters – S, A, r_{bp}, θ_{bp}, φ_{bp}, θ_w, φ_w, ζ_w – in terms of the row and column positions of the whiskers (Towal et al., 2011). However, parameterizing in terms of row and column does not permit vibrissal arrays to be compared across species because different animals have different numbers of whiskers. An alternative approach, taken in Belli et al., 2018, is to use the basepoint coordinates θ_{bp} and φ_{bp} as independent variables to quantify the other six parameters that define the array morphology.

Here we use this approach to quantify the whisker array of the harbor seal. Specifically, we quantify r_{bp}, S, A, θ_w, φ_w, ζ_w in terms of the variables θ_{bp} and φ_{bp}. We first describe the overall size and shape of the seal mystacial pad and then consider each of these six variables in turn.

3.2. The overall size and shape of the mystacial pad of the harbor seal

The whisker basepoints encompass a surface area ~23.1 cm^2 on the cheek of the seal (Fig. 3AB). To gain intuition for array size, it is helpful to compare the seal array to that of the rat (Fig. 3C). The seal's array is approximately 23 times larger in surface area of the rat's array, in which the basepoints occupy an area of ~1.02 cm^2. The seal array also spans a greater medial-lateral extent on the muzzle, so that its most rostral whiskers have larger values of θ_w. The most rostral whiskers of the seal cross 180° (c.f., Fig. 2E) and point inward toward the midline of the head.

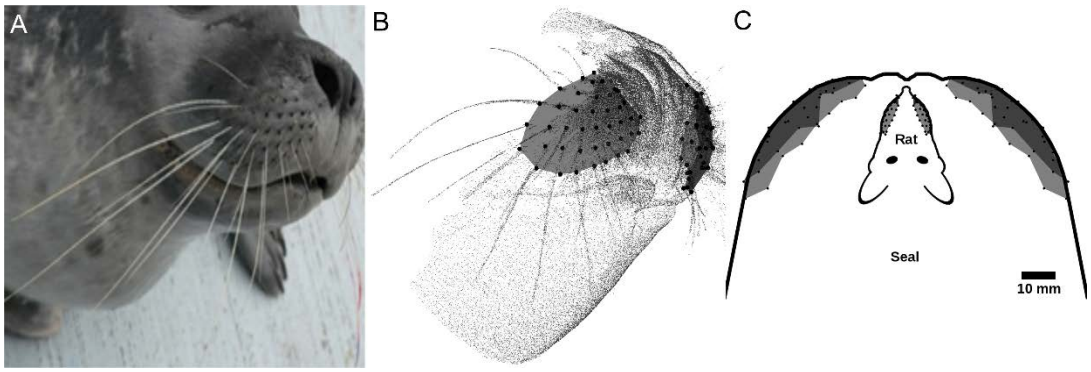

Fig. 3: Images of the harbor seal mystacial pad show the overall size and shape of the whisker array. A) A photograph of the seal mystacial pad and whiskers. **B)** The basepoint surface (a trimesh of the whisker basepoints) is overlaid on the 3D scanned point cloud. **C)** Top-down views that compare the rat and seal arrays.

3.2 Basepoint coordinates

Whisker identities within the seal array as well as the general array shape have been characterized in previous studies (Dehnhardt and Kaminski, 1995), and are shown in Fig. 4A. Plotting φ_{bp} vs. θ_{bp} yields a quantitative depiction of the array that closely resembles the qualitative description (Fig. 4B). In particular, the discontinuity in row direction between columns 4 and 5 is maintained in the quantitative description, although it is evidenced as a gradual bend in direction rather than a sudden break.

The basepoint coordinate θ_{bp} was used as an independent variable to quantify the radial coordinate of the basepoints (r_{bp}). Results are shown in Table 1 and show that r_{bp} did not depend on φ_{bp}. The final equation for r_{bp} as a function of θ_{bp} is:

$$r_{bp} = -0.4905\,\theta_{bp} + 36.489, \qquad \text{Adj. } R^2 : 0.834 \qquad \text{(eq. 1)},$$

where θ_{bp} is in degrees and r_{bp} is in millimeters. The 95% confidence intervals for the θ_{bp} coefficient and intercept are [-0.5236, -0.4574] and [35.8804, 37.0967] respectively. Note that equation 1 is only valid for the right side of the seal's face, where θ_{bp} varies between -90° (ventral) to +90° (dorsal). Results must be mirrored about the y-axis to produce results for the left side.

Table 1. Best fit equation for r_{bp} by individual animal.

Best Equation Fits for Individual Seals							
	Coefficients			95% Confidence Intervals			
(171 whiskers)	c_1	c_2	c_3	c_1	c_2	c_3	Adj. R^2
Seal 1 (56)	N/A	-0.42203	36.525	N/A	[-0.4729, -0.3711]	[35.5827, 37.4682]	0.833
Seal 2 (62)	0.003283	-0.53157	35.899	[4.970e-04, 0.0060702]	[-0.5945, -0.4687]	[34.6273, 37.1707]	0.838
Seal 3 (53)	0.004162	-0.61645	35.195	[0.001343, 0.006980]	[-0.6877, -0.5452]	[33.8951, 36.4957]	0.882
Combined	N/A	-0.4905	36.489	N/A	[-0.5236, -0.4574]	[35.8804, 37.0967]	0.846
Final equation: $r_{bp} = c_1\theta_{bp}^2 + c_2\theta_{bp} + c_3$, where r_{bp} is in millimeters and θ_{bp} is in degrees.							

Equation 1 indicates that r_{bp} decreases from caudal to rostral. This trend is depicted in Fig. 4C and is primarily caused by the orientation of the seal's mystacial pad. The pad is nearly vertical in the dorsoventral direction, so φ_{bp} does not contribute to changes in r_{bp}. In contrast, the mystacial pad varies considerably in the mediolateral direction, so r_{bp} varies systematically with θ_{bp}.

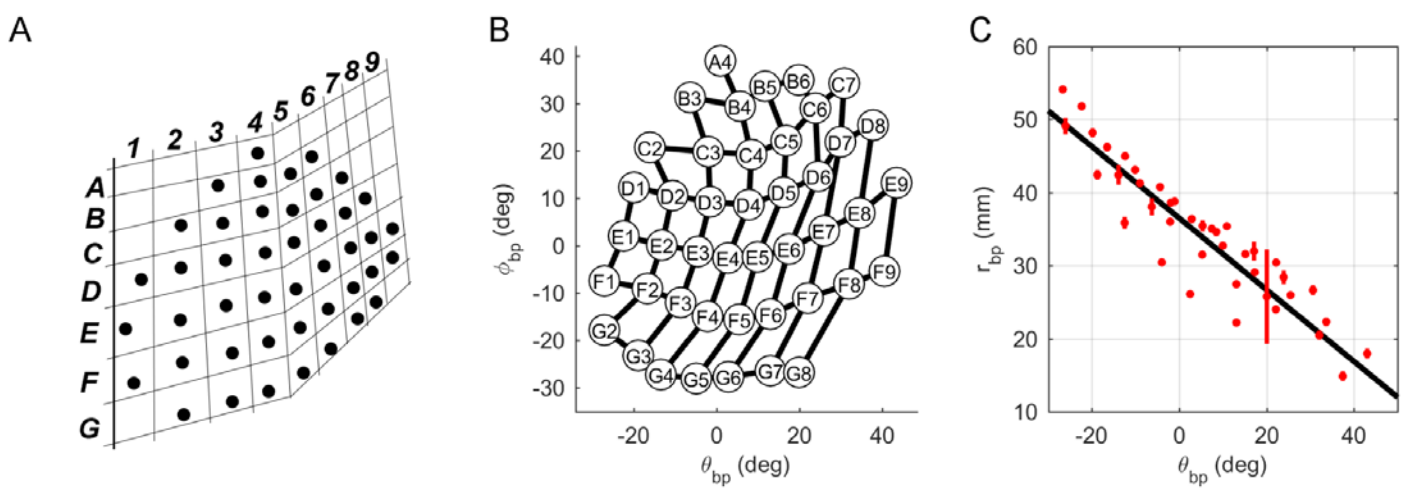

Fig. 4: The locations of the whisker basepoints are described in spherical coordinates (r_{bp}, θ_{bp}, φ_{bp}). A) Qualitative description of the shape of the seal whisker array from previous studies. Figure is recreated from image provided in (Dehnhardt and Kaminski, 1995). **B)** Plotting φ_{bp} against θ_{bp} quantifies the geometry of the array in a manner that closely resembles the qualitative description in (A). **C)** Radial basepoint coordinate (r_{bp}) is plotted as a function of θ_{bp}. The black line represents Equation 1. The mean of r_{bp} when grouped by Row and Col identity is represented by the red dots, with the standard error shown as red vertical bars. In accordance with Equation 1, the value of r_{bp} increases with θ_{bp}, from rostral to caudal.

3.3 Two-dimensional shape: arc length and curvature

We used the basepoint coordinates θ_{bp} and φ_{bp} as independent variables to quantify variations in arc length (S) and intrinsic whisker curvature (A) across the array. To provide intuition for S and A, traces of the F-row of whiskers from a single seal (seal 1) are shown in black in Fig. 5A. In general, the whiskers decrease in length and increase slightly in intrinsic curvature from caudal to rostral, but there is considerable variability, especially for whiskers F4 and F5. A sense for the magnitude of the variability is provided in the red traces of Fig. 5A, which show whiskers F4 and F5 obtained from the two other seals.

When averaged across all animals, whisker arc length is best described as an exponential function of θ_{bp} and φ_{bp}.

$$S = \exp(-0.0321\,\theta_{bp} - 0.0114\,\varphi_{bp} + 3.764)\,, \qquad \text{Adj. } R^2 : 0.735 \qquad \text{(eq. 2a)}$$

where θ_{bp} and φ_{bp} are in degrees and S is in millimeters. The 95% confidence intervals for the θ_{bp}, φ_{bp} coefficients and intercept are [-0.0388, -0.0254], [-0.0155, -0.00728], and [3.6861, 3.8422] respectively. As for equation 1, equation 2a only holds for the right side, where θ_{bp} varies from -90° (caudal) to +90° (rostral) and φ_{bp} varies from -90° (ventral) to +90° (dorsal). Recall also that this fit was found using only the 2D data (44 whiskers) because the 3D laser scanner truncated the distal portions of the whiskers during the 3D scans.

Notice that Equation 2a has negative coefficients in front of both θ_{bp} and φ_{bp}. The negative coefficient in front of θ_{bp} confirms the impression from Fig. 5A that whiskers tend to decrease in length from caudal to rostral. The negative coefficient in front of φ_{bp} indicates that whisker length also tends to decrease from ventral to dorsal, though this dependence is considerably weaker than the dependence on θ_{bp}. In each local region of the array, a change in the value of θ_{bp} will cause the arc length to change considerably more than the equivalent change in φ_{bp}.

The exponential decrease of S with increases in θ_{bp} and φ_{bp} is shown in Fig. 5B, where the surface represents equations 2a and the red points are the mean value of S when grouped by whisker identity +/- the standard error. The surface shown in Fig. 5B is more intuitively represented by an alternative form of equation 2a:

$$S = \frac{43.1206}{\left(e^{0.0321\theta_{bp} + 0.0114\varphi_{bp}}\right)} \qquad \text{Adj. } R^2 : 0.735 \qquad \text{(eq. 2b)}$$

Equation 2b provides the intuition that S will equal ~43 mm in the middle of the array, where both θ_{bp} and φ_{bp} equal zero, and then vary exponentially in both directions from that central point.

Fig. 5C compares the arc length values predicted by equations 2ab with the raw measurements. A perfect model of the data would lie along the diagonal line (y = x) in the figure. Instead, the model underestimates the length of whiskers longer than ~60 mm, and whiskers shorter than ~60 mm are clustered with a relatively broad distribution about the diagonal. It seems likely that the prediction for arc length could be significantly improved with more data. Finally, Fig. 5D shows the equation 2ab prediction for S across the whisker array, confirming that the caudal and ventral-most whiskers are the longest.

We next turned to quantifying intrinsic whisker curvature, using the same 44 whiskers as were used to quantify 2D arc length. As described in *Methods*, the shape of the seal's whiskers were found to be well described by the function $y=Ax^3$, with the coefficient A termed the cubic curvature coefficient. When quantified in terms of basepoint parameters the value of A was not significant in φ_{bp}, so equation 3 expresses A only as a function of θ_{bp}:

$$A = 9.2327\text{e-}06\,\theta_{bp} + 0.00022015 \qquad \text{Adj. } R^2 : 0.667 \qquad \text{(eq. 3)}$$

In equation 3, θ_{bp} has units of degrees and A has units of $1/mm^2$.

However, further investigation found that whisker curvature was significantly better described as an exponential function of arc length rather than as a linear function of θ_{bp}, as seen in equation 4:

$$A = \exp(-0.030799\ S - 7.2348) \qquad \text{Adj. } R^2\text{: } 0.837 \qquad \text{(eq. 4)}$$

In equation 4, S has units of millimeters, and A has units of $1/mm^2$. The 95% confidence intervals for the arc length coefficient and intercept are [-0.0350, -0.0266] and [-7.4968, -6.9727] respectively. Consistent with the visual intuition provided in Fig. 5A, equations 3 and 4 indicate that shorter, more rostral whiskers typically have a higher curvature coefficient than the longer, more caudal whiskers.

Fig. 5E shows equation 4 as a solid black line plotted over the raw data points. Although the fit is excellent for whiskers with arc lengths greater than ~50 mm, there is considerably more scatter about the curve for whiskers with smaller arc lengths. This increased scatter is easily observed when the experimental values for A are compared with those predicted by equation 4 (Fig. 5F).

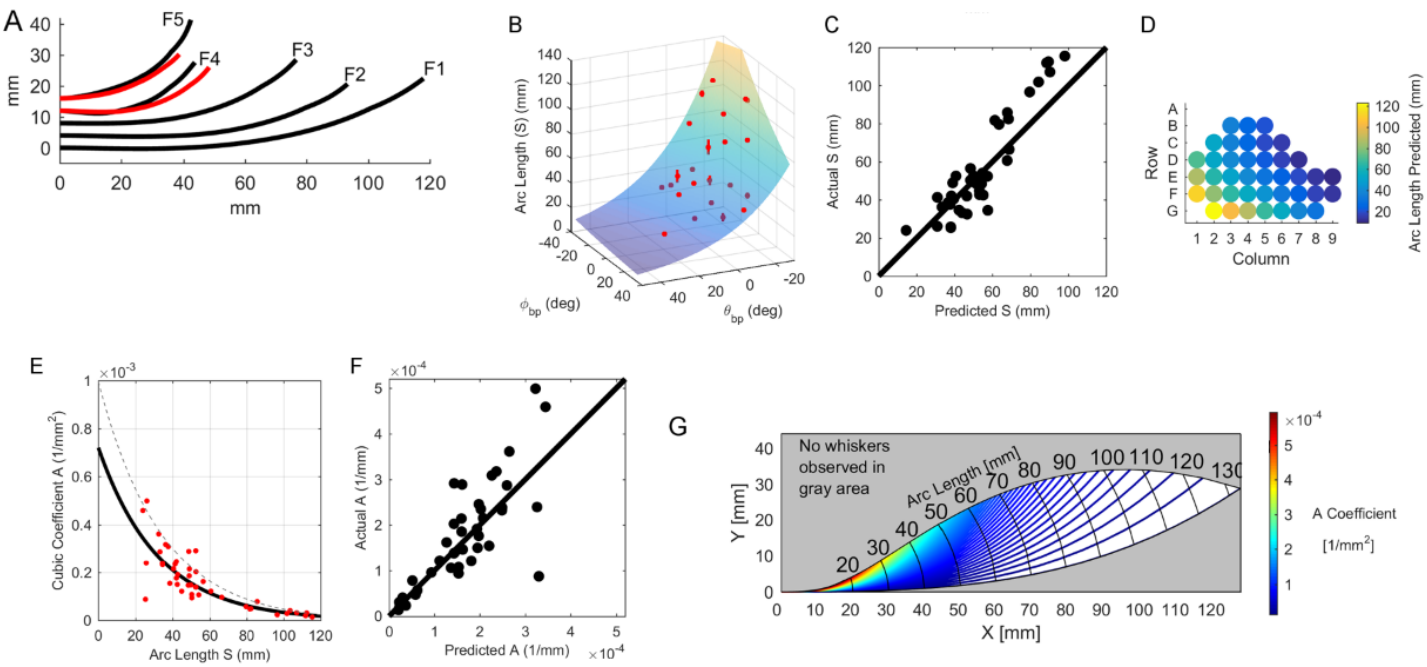

Fig. 5. Relationship between 2D whisker geometry and basepoint parameters θ_{bp} and φ_{bp}. (A) Black traces show the shapes of the F-row of whiskers from a single seal. Whiskers F4 and F5 from two other seals are shown in red to illustrate typical variability in arc length and curvature. (**B)** This subplot shows the surface described by equation 2. Arc length can be described as a decaying exponential function of both θ_{bp} and φ_{bp} from caudal to rostral and ventral to dorsal across the array. Mean ± standard error when grouped by whisker identity is shown in red. **(C)** Experimentally measured values for arc length are compared with values predicted from equation 2. The diagonal line y = x is shown in black. **(D)** A colormap shows how equation 2 predicts arc length will vary across the array. **(E)** The intrinsic curvature coefficient (*A)* can be described as an exponentially decreasing function of arc length. The solid black line represents equation 4 and the dashed gray line represents equation 5. Red points represent raw values from the 44 whiskers. **(F)** Experimentally measured values for the curvature coefficient are compared with values predicted from equation 4. The diagonal line y = x is shown in black. Notice that the prediction decreases in quality as *A* increases. **(G)** A mock dataset was generated to illustrate the full range of possible whisker shapes and explore the variability seen in (E). Each black arc represents a whisker of a particular length (20 mm, 30 mm, etc…). The whisker shapes are drawn in colors that indicate their curvature coefficients. Following along the black arcs, it is clear that a small change in tip location of a short whisker will cause a large change in the curvature coefficient. A small change in tip location of a long whisker will cause only a small change in the curvature coefficient.

To explain the increased variability for the shorter whiskers, we constructed a set of mock data in three steps. First, we determined the minimum and maximum values of A found in the experimental dataset. Second, we found the upper bound on the relationship between the curvature coefficient and arc length. This bound is shown as a thin, dashed, gray line in figure 5E, and is given by the equation:

$$A = 0.001002 * \exp(-0.02961\ S) - 0.000005437 \qquad \text{(eq. 5a)}$$

Inverting this relationship to find S as a function of A gives:

$$S = \left(\frac{-1}{0.02961}\right) log\left(\frac{A+0.000005437}{0.001002}\right) \qquad \text{(eq. 5b)}$$

Third, the set of mock whisker shapes is created by choosing A values between the minimum and maximum in increments of 5.8×10^{-6} and inserting those values into the equation $y=Ax^3$. Equation 5b is then used to calculate the arc length and truncate the whisker to the appropriate length.

The shapes of the whiskers in the mock dataset are shown in Figure 5G, and reveal important features of the relationship between S and A. For short whiskers, even a tiny change in the location of the whisker tip has a very large effect on the curvature coefficient. In contrast, for long whiskers, a small change in the location of the whisker tip has only a small effect on the curvature coefficient. In other words, the sensitivity of the A coefficient model depends strongly on the arc length of this whisker. This effect explains the high variability for short whiskers in Fig. 5E. In addition, there are clear regions (shaded gray) in which no whiskers are found. The lower bound prevents the whisker from being perfectly straight. The upper bound limits the y-coordinate of the whisker's tip in Figure 5G, which could prevent whiskers from overlapping each other too much when oriented in the array.

3.4 Angles of emergence of the whiskers on the mystacial pad of the seal

Finally, we used the basepoint coordinates θ_{bp} and φ_{bp} as independent variables to quantify the angles of emergence of the whiskers across the array. As shown in Table 2, the best fit equations for θ_w and ζ_w were linear in both θ_{bp} and φ_{bp}, while the best fit equation for φ_w depended only on φ_{bp}. The final equations for the angles of emergence were:

$$\theta_w = 1.770\ \theta_{bp} - 1.100\ \varphi_{bp} + 138.42 \qquad \text{Adj. } R^2\text{: } 0.854 \qquad \text{(eq. 5)}$$

$$\varphi_w = 1.570\ \varphi_{bp} - 20.928 \qquad \text{Adj. } R^2\text{: } 0.875 \qquad \text{(eq. 6)}$$

$$\zeta_w = 1.866\ \theta_{bp} - 1.540\ \varphi_{bp} - 24.447 \qquad \text{Adj. } R^2\text{: } 0.784 \qquad \text{(eq. 7)}$$

In equations 5, 6, and 7, all variables have units of degrees. Fig. 6 shows the three angles of emergence as functions of θ_{bp} and φ_{bp}.

Table 2. Best fit equations for the angles of emergence by individual animal.

	Coefficients				95% Confidence Intervals				Adj. R^2
	c_1	c_2	c_3	c_4	c_1	c_2	c_3	c_4	
θ_w									
Seal 1 (56)	N/A	-0.972	1.815	133.02	N/A	[-1.1597, -0.7849]	[1.6454, 1.9849]	[129.9012, 136.1351]	0.903
Seal 2 (62)	N/A	-1.141	1.647	138.42	N/A	[-1.3181, -0.9631]	[1.4731, 1.8199]	[135.3208, 141.5222]	0.889
Seal 3 (53)	0.0504	-0.749	1.856	133.85	[0.0394, 0.0615]	[-0.9656, -0.5319]	[1.6882, 2.0236]	[129.8400, 137.8607]	0.923
Combined (171)	N/A	-1.100	1.770	138.42	N/A	[-1.2346, -0.9655]	[1.6481, 1.8927]	[136.1603, 140.6733]	0.854
Final equation: $\theta_w = c_1\varphi_{bp}^2 + c_2\varphi_{bp} + c_3\theta_{bp} + c_4$, where θ_w, φ_{bp} and θ_{bp} are in degrees.									
φ_w									
Seal 1 (56)	N/A	1.700	N/A	-23.345	N/A	[1.5198, 1.8800]	N/A	[-26.3311, -20.3596]	0.867
Seal 2 (62)	N/A	1.449	N/A	-21.738	N/A	[1.3460, 1.5526]	N/A	[-23.4949, -19.9809]	0.928
Seal 3 (53)	0.0127	1.730	N/A	-19.799	[0.003515, 0.02179]	[1.5494, 1.9098]	N/A	[-22.9582, -16.6397]	0.882
Combined (171)	N/A	1.570	N/A	-20.928	N/A	[1.4802, 1.6597]	N/A	[-22.3935, -19.4632]	0.875
Final equation: $\varphi_w = c_1\varphi_{bp}^2 + c_2\varphi_{bp} + c_3\theta_{bp} + c_4$, where φ_w, φ_{bp}, and θ_{bp} are in degrees.									
ζ_w									
Seal 1 (56)	N/A	-1.350	1.573	-23.663	N/A	[-1.7195, -0.9803]	[1.2382, 1.9078]	[-29.8110, -17.5155]	0.693
Seal 2 (62)	N/A	-1.565	1.753	-23.714	N/A	[-1.8397, -1.2893]	[1.4836, 2.0214]	[-28.5220, -18.9053]	0.818
Seal 3 (53)	N/A	-1.732	2.308	-28.091	N/A	[-2.1166, -1.3482]	[1.9916, 2.6238]	[-34.2624, -21.9194]	0.840
Combined (171)	N/A	-1.540	1.866	-24.447	N/A	[-1.7351, -1.3448]	[1.6882, 2.0429]	[-27.7197, -21.1746]	0.784
Final equation: $\zeta_w = c_1\varphi_{bp}^2 + c_2\varphi_{bp} + c_3\theta_{bp} + c_4$, where ζ_w, φ_{bp}, and θ_{bp} are in degrees.									

As shown in Fig. 6A and consistent with the signs of the coefficients for θ_{bp} and φ_{bp} in equation 5, the angle θ_w increases from caudal to rostral across the array and decreases from ventral to dorsal. The most rostral whiskers point forward and inward (~200°) while the caudal whiskers point slightly backwards (~60°). Relatively uniform dispersion of actual vs. predicted values for θ_w about the line y = x in Fig. 6B indicates selction of the correct model for equation 5. Variation in θ_w across the array (calculated from equation 5) is shown as a colormap in Fig. 6C and confirms the observation in Fig. 6A that the rostral and ventral-most whiskers point forwards, while the caudal and dorsal whiskers point slightly backwards.

A similar analysis is performed for φ_w in Figures 6D-F, with the difference that the angle φ_w is a function only of a single variable (φ_{bp}) and does not depend on θ_{bp}. As shown in Fig. 6D, φ_w increases from ventral to dorsal across the array, with no significant change in the caudal-rostral direction. The dorsal whiskers point up (~40°) while the ventral whiskers point down (~-60°). Notably, the φ_w angles are not symmetric about 0°, indicating that the whiskers are skewed to point downward. When actual vs. predicted values for φ_w are plotted (Fig. 6E) the points are relatively uniformly dispersed about the line of equality, indicating selection of the correct model for equation 6. Finally, the prediction for variation in φ_w across the array confirms the ventral-dorsal trend observed in Fig. 6D.

Similar to the trends for θ_w, Fig. 6G and equation 7 indicate that ζ_w increases moving caudal to rostral across the array and decreases moving in the ventral to dorsal direction. The caudal/dorsal whiskers point the most concave backwards, and the rostral/ventral whiskers point the most concave forward and inward. However, the ζ_w angles have standard error values that are higher than those for θ_w and φ_w. The reason for the higher error is due to the intrinsic nature of measuring ζ_w about the whiskers' own axis, which is especially error prone for short and/or straight whiskers. Relatively uniform dispertion of actual vs. predicted values for ζ_w about the line y = x in Fig. 6H indicates selection of the correct model used in Fig. 6G (equation 7). Finally, Fig. 6I illustrates a "diagonal" trend in ζ_w across the array, as predicted from equation 7. Notably, the pattern of variation for ζ_w is strikingly similar to that of θ_w (compare Fig. 6I with Fig. 6C). These two variables are closely linear with r = 0.875 (Pearson correlation).

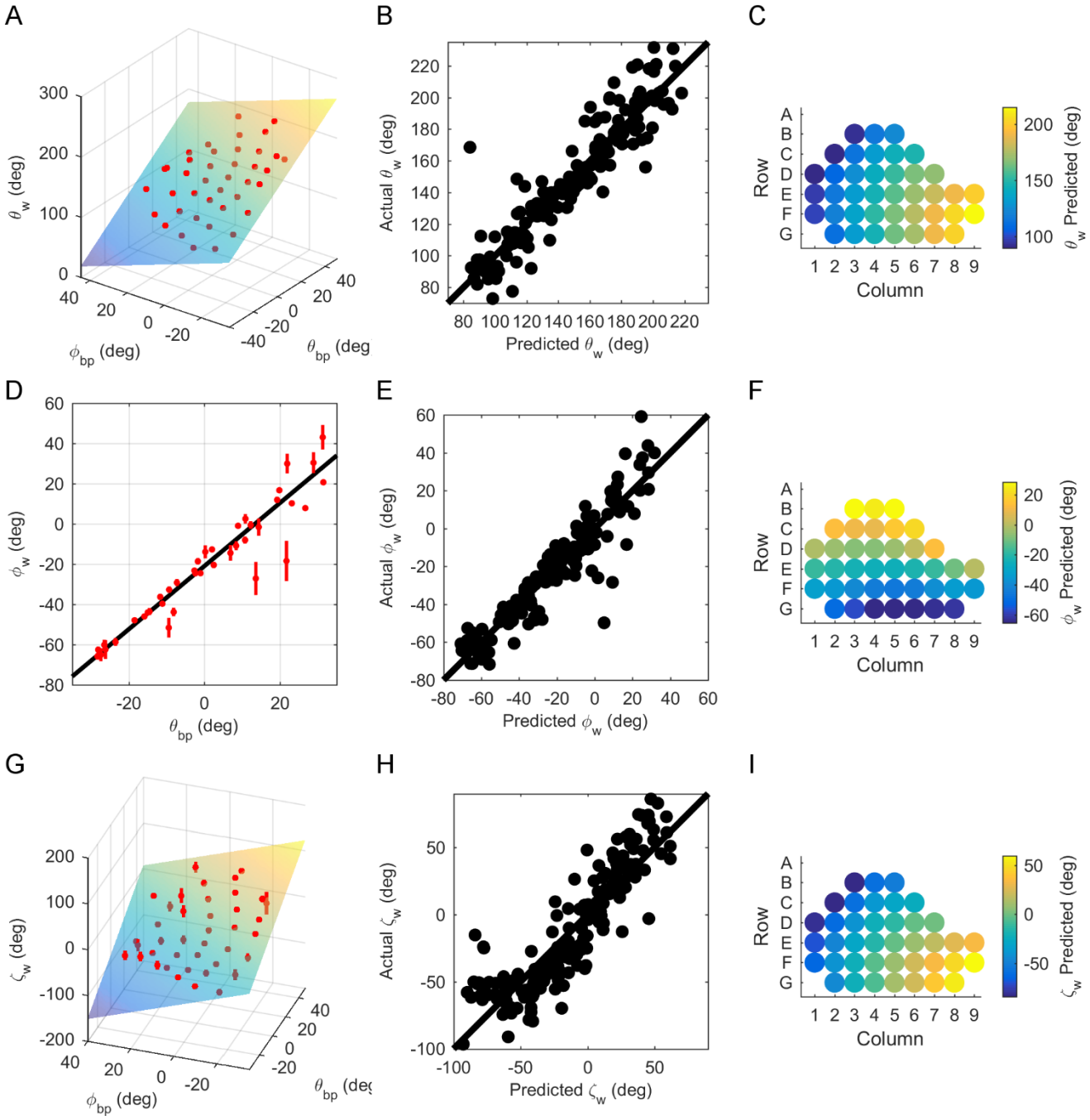

Fig. 6: Relationship between whisker angles of emergence and basepoint parameters. **A)** Theta Euler (θ_w) can be described as a linear function of θ_{bp} and φ_{bp} (eq. 5). Mean ± standard error when grouped by whisker identity is shown in red. **B)** Relatively uniform dispertion of actual vs. predicted values for θ_w about the line y = x indicates selection of the correct model used in (A) **C)** Prediction of θ_w by whisker identity using equation 5. **D)** Phi Euler (φ_w) can be described as a linear function of φ_{bp} (eq. 6). Mean ± standard error when grouped by whisker identity is shown in red. **E)** Relatively uniform dispertion of actual vs. predicted values for φ_w about the line y = x indicates selection of the correct model used in (D). **F)** Prediction of φ_w by whisker identity using equation 6. **G)** Zeta Euler (ζ_w) can be described as a polynomial function linear in φ_{bp} and linear in θ_{bp} (eq. 7). Mean ± standard error when grouped by whisker identity is shown in red. **H)** Relatively uniform dispertion of actual vs. predicted values for ζ_w about the line y = x indicates selection of the correct model used in (G). **I)** Prediction of ζ_w across the array using equation 7.

3.5 The full model of the seal array

The equations shown in the previous sections are summarized in Table 3, and, taken together, can be used to generate a full model of the seal vibrissal array. A 3D CAD model based on these equations is shown in Fig. 7A. Using the portions of the 3D point clouds that were discarded previously (the face and neck) a model of the seal's head was also created. The final model can be compared to photographs of real seals shown in Fig. 7B.

Table 3. Equations describing the morphology of the seal vibrissal array.

Parameter	Description	Equation
$\mathbf{r_{bp}}$	Radial coordinate of the basepoint	$\mathbf{r_{bp}} = -0.4905\ \theta_{bp} + 36.489$
S	Arc length	$\mathbf{S} = \exp(-0.0321\ \theta_{bp} - 0.0114\ \varphi_{bp} + 3.764)$
A	Cubic coefficient	$\mathbf{A} = A = \exp(-0.030799\ S - 7.2348)$
$\boldsymbol{\theta_w}$	Azimuthal angle of emergence	$\boldsymbol{\theta_w} = 1.770\ \theta_{bp} - 1.100\ \varphi_{bp} + 138.42$
φ_w	Elevation angle of emergence	$\boldsymbol{\varphi_w} = 1.570\ \varphi_{bp} - 20.928$
$\boldsymbol{\zeta_w}$	Roll angle of emergence	$\boldsymbol{\zeta_w} = 1.866\ \theta_{bp} - 1.540\ \varphi_{bp} - 24.447$

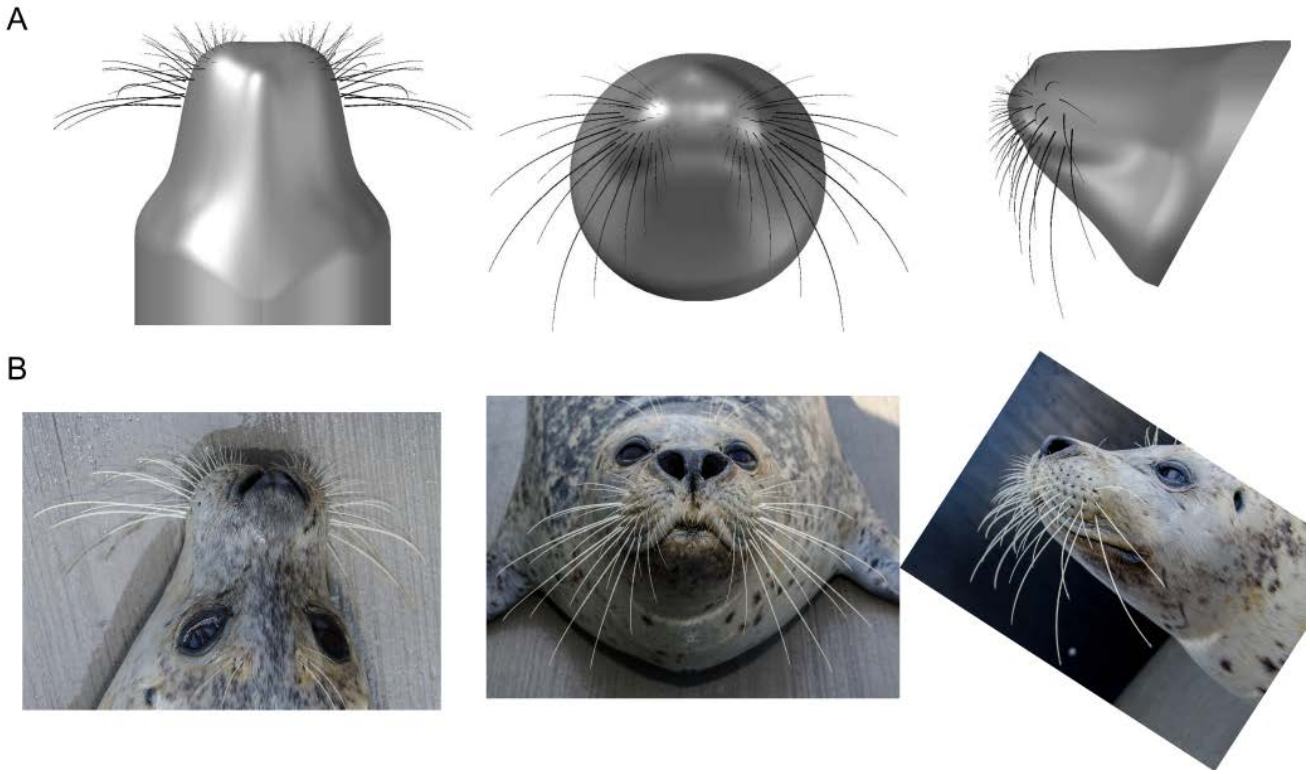

Fig. 7: The model of the seal whisker array is compared with photographs of the seal.

4. Discussion

Previous work has characterized the shape, size, and flexural stiffness of individual seal whiskers (Ginter et al., 2012; Ginter et al., 2010; Murphy et al., 2013; Summarell et al., 2015), as well as the detailed anatomy of the whisker follicle complex (Dehnhardt et al., 1999; Dykes, 1975). We now add to these data by characterizing the overall three dimensional arrangement (position and orientation) of the whiskers across the mystacial pad.

4.1. Varying arc length and curvature of whiskers across the array may confer aquatic-sensing advantages

The present results quantify the visual intuition that vibrissal arc length varies systematically across the array, with length increasing exponentially from rostral to caudal. Given that the resonant modes of a fixed-free tapered cantilever beam are inversely related to the beam's length (Georgian, 1965), these data predict that the more rostral, shorter vibrissae will respond more strongly to higher frequencies, while the longer, caudal whiskers will respond more strongly to lower frequencies. Thus the vibrissal array could morphologically compute the frequency spectrum of flow disturbances. If a particular animal or moving object leaves a hydrodynamic trail with a characteristic frequency signature, the seal may be able to identify not only the location of the trail but also the identity of the object.

While rat whiskers are best described by a quadratic function (Belli et al., 2018; Knutsen et al., 2008; Towal et al., 2011), seal whiskers are better described by a cubic fit. They do not start to curve appreciably until relatively far from the base (Fig. 5A), resulting in a nearly straight proximal portion. In addition, longer seal whiskers have, on average, lower intrinsic curvature than shorter whiskers (Fig. 5E), so that that the longest, most caudal whiskers tend also to be the straightest. The placement and length of these whiskers means that they may be especially useful in expanding the animal's search space for detecting escaping fish and targeting bites.

4.2. The orientation of the whisker on the head: "curvature orientation" is different from "diameter orientation"

The whiskers of many marine mammals have elliptical cross-sections, and studies have often defined the "orientation" of the whisker based on which side of the whisker has the large diameter(Ginter et al., 2010; Miersch et al., 2011; Murphy et al., 2013). In contrast, the whiskers of terrestrial mammals tend to have circular cross sections, and studies have defined whisker "orientation" based on the orientation of the whisker's intrinsic curvature (Belli et al., 2018; Knutsen et al., 2008; Quist and Hartmann, 2012; Towal et al., 2011). It is, therefore, critical to keep "curvature-orientation" distinct from "diameter-orientation," as these two different geometric features will have independent effects on the whisker's mechanical response to flow.

In the harbor seal, the intrinsic curvature of the whisker aligns with the major axis of the whisker and the flexural stiffness along the major axis is nearly double that of the minor axis (Summarell et al., 2015). In contrast, sea lion whiskers have an intrinsic curvature aligned with their minor diameter axis (Murphy et al., 2013). Thus in both species, the intrinsic curvature and diameter covary, but in opposite directions. Future studies will need to identify the relationships between these two parameters in other species.

4.3. Seal whiskers may be evolutionary selected to control for multiple sources of vibration

Vortex-induced vibrations of the whisker are thought to be a major source of noise for seals during wake tracking, and undulations along the whisker length reduce these vibrations (Ginter et al., 2012; Hanke et al., 2010). The current study now quantifies the orientation of the whiskers intrinsic curvature (ζ_w), which, along with diameter-orientation, will also affect vibration magnitude. With the head pitched to ensure that the average row plane is horizontal (Fig. 2B), the angle ζ_w varies between ~-90 and ~60 degrees (Fig 6). Thus the more caudal whiskers are oriented concave backwards, while the more rostral whiskers are oriented concave down. In contrast, the rat whisker array has considerably more whiskers oriented concave forwards (Belli et al., 2018; Knutsen et al., 2008; Quist and Hartmann, 2012; Towal et al., 2011).

Vibrations of the whisker will be strongly affected not only by ζ_w , but also by θ_w, the angle at which the whiskers emerge in the rostro-caudal plane. Changes in θ_w effectively change the area projected into the flow, and will consequently change how the whisker vibrates. Thus both ζ_w and θ_w will affect the whiskers mechanical response. Intriguingly, for the seal -- but not for the rat -- the two angles θ_w and ζ_w are strongly correlated across the array (Figure 6C and 6I). By varying these two angles virtually in lock step across the array, the seal vibrissal

system may effectively ensure that these two different sources of vibration variability are always related in the same way.

4.4. An approach to the quantification of facial morphology across species

Although the present work had as its primary goal the morphological quantification of the seal whisker array, it also more generally continues our ongoing investigations of the variable morphologies of whiskered animals. We anticipate that comparative studies will reveal that vibrissal array morphologies are optimized for particular behaviors, but adequate for many behaviors.

For example, seals use their whiskers not only for hydrodynamic tracking but also for tactile object discrimination through direct contact, similar to a rat (Dehnhardt and Kaminski, 1995; Grant et al., 2013a). Conversely, recent studies have found that rats use their whiskers not only for direct tactile discriminations, but during anemotaxic behaviors (Yu et al., 2016a; Yu et al., 2016b). We hypothesize that the whisker arrays of animals are shaped for their primary behavioral tasks, but that even sub-optimal morphology can be used for secondary tasks. We expect that the whisker arrays of semi-aquatic species (otters, beavers, water rats) will lie somewhere between terrestrial and aquatic mammals, sacrificing optimality for versatility.

Thus, although we expect whisker array morphology to be related to species-specific ecological niche and behavior, we also expect common selective pressures to generate a “basic whisker plan” even across distantly related species. Future comparative studies will help address this question.

ACKNOWLEDGMENTS

We thank Dr. Chris S. Bresee for helpful discussions, insights, and critiques, and Dr. Christine Scholtyßeck for help handling the seals. E. Claire Mosier, an undergraduate student in Northwestern’s Biomedical Engineering department, helped us take some of the data in Rostock. We are grateful to RAPIDFORM™ for providing a temporary stand-alone license to acquire and analyze the scans when we briefly lost access to the internet at a critical point in the work. Portions of this work have been published in two Ph.D. dissertations: Graff, MM (2016) *Mechanisms of Whisker Based Flow Sensing*, Ph.D. Thesis, Northwestern University. ProQuest/UMI, 130 pages (Publication No. 10160640). Belli, HM (2017) *Sensing with Whiskers: From Geometry and Mechanics to the Statistics of the Array*, Ph.D. Thesis, Northwestern University, ProQuest/UMI, 253 pages; (Publication No. 10681095).

COMPETING INTERESTS

No competing interests declared.

FUNDING

This multi-year research project was sequentially supported by NSF awards IOS-0846088, CRCNS-IIS-1208118, and BCS-1734981 to MJZH, by a grant from the VolkswagenStiftung to GD, and by a grant from the German Research Foundation (SPP1207) to GD (DE 538/9-2) and W. Hanke (HA 4411/8-1). HMB was supported in part by a Ruth L. Kirschstein Predoctoral Individual NRSA, NIH F31-NS-090872-01A1.

References

Arkley, K., Grant, R. A., Mitchinson, B. and Prescott, T. J. (2014). Strategy change in vibrissal active sensing during rat locomotion. *Current Biology* **24**, 1507-1512.

Belli, H. M., Bresee, C. S., Graff, M. M. and Hartmann, M. J. Z. (2018). Quantifying the three-dimensional facial morphology of the laboratory rat with a focus on the vibrissae. *PLoS One* **13**, 31.

Brecht, M., Preilowski, B. and Merzenich, M. M. (1997). Functional architecture of the mystacial vibrissae. *Behavioural Brain Research* **84**, 81-97.

Danforth, C. (1925). Hair in its relation to questions of homology and phylogeny. *American Journal of Anatomy* **36**, 47-68.

Dehnhardt, G., Hyvarinen, H., Palviainen, A. and Klauer, G. (1999). Structure and innervation of the vibrissal follicle-sinus complex in the australian water rat, *Hydromys chrysogaster*. *Journal of Comparative Neurology* **411**, 550-562.

Dehnhardt, G. and Kaminski, A. (1995). Sensitivity of the mystacial vibrissae of harbor seals (*Phoca vitulina*) for size differences of actively touched objects. *Journal of Experimental Biology* **198**, 2317-2323.

Dehnhardt, G., Mauck, B. and Bleckmann, H. (1998). Seal whiskers detect water movements. *Nature* **394**, 235-236.

Dehnhardt, G., Mauck, B., Hanke, W. and Bleckmann, H. (2001). Hydrodynamic trail-following in harbor seals (*Phoca vitulina*). *Science* **293**, 102-104.

Dykes, R. W. (1975). Afferent-fibers from mystacial vibrissae of cats and seals. *Journal of Neurophysiology* **38**, 650-662.

Georgian, J. (1965). Vibration frequencies of tapered bars and circular plates. *J Appl Mech* **32**, 234–235.

Ginter, C. C., DeWitt, T. J., Fish, F. E. and Marshall, C. D. (2012). Fused traditional and geometric morphometrics demonstrate pinniped whisker diversity. *PLoS One* **7**.

Ginter, C. C., Fish, F. E. and Marshall, C. D. (2010). Morphological analysis of the bumpy profile of phocid vibrissae. *Marine Mammal Science* **26**, 733-743.

Grant, R., Wieskotten, S., Wengst, N., Prescott, T. and Dehnhardt, G. (2013a). Vibrissal touch sensing in the harbor seal (*Phoca vitulina*): How do seals judge size? *Journal of Comparative Physiology a-Neuroethology Sensory Neural and Behavioral Physiology* **199**, 521-533.

Grant, R. A., Breakell, V. and Prescott, T. J. (2018). Whisker touch sensing guides locomotion in small, quadrupedal mammals. *Proceedings of the Royal Society B-Biological Sciences* **285**, 9.

Grant, R. A., Haidarliu, S., Kennerley, N. J. and Prescott, T. J. (2013b). The evolution of active vibrissal sensing in mammals: Evidence from vibrissal musculature and function in the marsupial opossum *Monodelphis domestica*. *Journal of Experimental Biology* **216**, 3483-3494.

Grant, R. A., Mitchinson, B., Fox, C. W. and Prescott, T. J. (2009). Active touch sensing in the rat: Anticipatory and regulatory control of whisker movements during surface exploration. *Journal of Neurophysiology* **101**, 862-874.

Grant, R. A., Mitchinson, B. and Prescott, T. J. (2012). The development of whisker control in rats in relation to locomotion. *Developmental Psychobiology* **54**, 151-168.

Haidarliu, S., Bagdasarian, K., Shinde, N. and Ahissar, E. (2017). Muscular basis of whisker torsion in mice and rats. *Anatomical Record-Advances in Integrative Anatomy and Evolutionary Biology* **300**, 1643-1653.

Haidarliu, S., Kleinfeld, D., Deschenes, M. and Ahissar, E. (2015). The musculature that drives active touch by vibrissae and nose in mice. *Anatomical Record-Advances in Integrative Anatomy and Evolutionary Biology* **298**, 1347-1358.

Haidarliu, S., Simony, E., Golomb, D. and Ahissar, E. (2010). Muscle architecture in the mystacial pad of the rat. *Anatomical Record-Advances in Integrative Anatomy and Evolutionary Biology* **293**, 1192-1206.

Haidarliu, S., Simony, E., Golomb, D. and Ahissar, E. (2011). Collagenous skeleton of the rat mystacial pad. *Anatomical Record-Advances in Integrative Anatomy and Evolutionary Biology* **294**, 764-773.

Hanke, W., Witte, M., Miersch, L., Brede, M., Oeffner, J., Michael, M., Hanke, F., Leder, A. and Dehnhardt, G. (2010). Harbor seal vibrissa morphology suppresses vortex-induced vibrations. *Journal of Experimental Biology* **213**, 2665-2672.

Hill, D. N., Bermejo, R., Zeigler, H. P. and Kleinfeld, D. (2008). Biomechanics of the vibrissa motor plant in rat: Rhythmic whisking consists of triphasic neuromuscular activity. *Journal of Neuroscience* **28**, 3438-3455.

Hirons, A. C., Schell, D. M. and St Aubin, D. J. (2001). Growth rates of vibrissae of harbor seals (phoca vitulina) and steller sea lions (*Eumetopias jubatus*). *Canadian Journal of Zoology-Revue Canadienne De Zoologie* **79**, 1053-1061.

Hobbs, J. A., Towal, R. B. and Hartmann, M. J. Z. (2016). Evidence for functional groupings of vibrissae across the rodent mystacial pad. *Plos Computational Biology* **12**, 36.

Hyvarinen, H. (1989). Diving in darkness - whiskers as sense-organs of the ringed seal (*Phoca hispida saimensis*). *Journal of Zoology* **218**, 663-678.

Jin, T. E., Witzemann, V. and Brecht, M. (2004). Fiber types of the intrinsic whisker muscle and whisking behavior. *Journal of Neuroscience* **24**, 3386-3393.

Knutsen, P. M., Biess, A. and Ahissar, E. (2008). Vibrissal kinematics in 3d: Tight coupling of azimuth, elevation, and torsion across different whisking modes. *Neuron* **59**, 35-42.

Kruger, Y., Hanke, W., Miersch, L. and Dehnhardt, G. (2018). Detection and direction discrimination of single vortex rings by harbour seals (*Phoca vitulina*). *Journal of Experimental Biology* **221**, 12.

Miersch, L., Hanke, W., Wieskotten, S., Hanke, F. D., Oeffner, J., Leder, A., Brede, M., Witte, M. and Dehnhardt, G. (2011). Flow sensing by pinniped whiskers. *Philosophical Transactions of the Royal Society B-Biological Sciences* **366**, 3077-3084.

Muchlinski, M. N. (2010). A comparative analysis of vibrissa count and infraorbital foramen area in primates and other mammals. *Journal of Human Evolution* **58**, 447-473.

Murphy, C. T., Eberhardt, W. C., Calhoun, B. H., Mann, K. A. and Mann, D. A. (2013). Effect of angle on flow-induced vibrations of pinniped vibrissae. *PLoS One* **8**.

Quist, B. W. and Hartmann, M. J. Z. (2012). Mechanical signals at the base of a rat vibrissa: The effect of intrinsic vibrissa curvature and implications for tactile exploration. *Journal of Neurophysiology* **107**, 2298-2312.

Schulte-Pelkum, N., Wieskotten, S., Hanke, W., Dehnhardt, G. and Mauck, B. (2007). Tracking of biogenic hydrodynamic trails in harbour seals (*Phoca vitulina*). *Journal of Experimental Biology* **210**, 781-787.

Summarell, C. C. G., Ingole, S., Fish, F. E. and Marshall, C. D. (2015). Comparative analysis of the flexural stiffness of pinniped vibrissae. *PLoS One* **10**.

Towal, R. B. and Hartmann, M. J. Z. (2008). Variability in velocity profiles during free-air whisking behavior of unrestrained rats. *Journal of Neurophysiology* **100**, 740-752.

Towal, R. B., Quist, B. W., Gopal, V., Solomon, J. H. and Hartmann, M. J. Z. (2011). The morphology of the rat vibrissal array: A model for quantifying spatiotemporal patterns of whisker-object contact. *PLoS Computational Biology* **7**.

Welker, W. (1964). Analysis of sniffing of the albino rat. *Behaviour* **22**, 223 – 244.

Wieskotten, S., Dehnhardt, G., Mauck, B., Miersch, L. and Hanke, W. (2010). Hydrodynamic determination of the moving direction of an artificial fin by a harbour seal (*Phoca vitulina*). *Journal of Experimental Biology* **213**, 2194-2200.

Wieskotten, S., Mauck, B., Miersch, L., Dehnhardt, G. and Hanke, W. (2011). Hydrodynamic discrimination of wakes caused by objects of different size or shape in a harbour seal (*Phoca vitulina*). *Journal of Experimental Biology* **214**, 1922-1930.

Woolsey, T., Welker, C. and Schwartz, R. (1975). Comparative anatomical studies of the sml face cortex with special reference to the occurrence of “barrels” in layer IV. *Journal of Comparative Neurology* **164**, 79-94.

Yu, Y. S. W., Graff, M. M. and Hartmann, M. J. Z. (2016). Mechanical responses of rat vibrissae to airflow. *Journal of Experimental Biology* **219**, 937-948.

Yu, Y. S. W., Graff, M. M., Bresee, C. S., Man, Y. B. and Hartmann, M. J. Z. (2016b). Whiskers aid anemotaxis in rats. *Science Advances* **2**, 7.